Nickel-doped zinc oxide thin films made by spray pyrolysis: experimental characterization and theoretical analyses

M. Bolino[1], D. Richard[1,2], M. R. Tejerina[1,2]*
[1]Universidad Nacional de La Plata, Buenos Aires, Argentina
[2]Centro de Tecnología de Recursos Minerales y Cerámica (CIC-CONICET-CCT La Plata-UNLP), Cno. Centenario y 506 s/n, C.C. 49 (B1897ZCA), M.B. Gonnet, Argentina

Abstract

A study of ZnO-based ceramic films prepared by the spray-pyrolysis technique is presented. Pure and Ni-doped thin film samples were deposited as a coating on a glass substrate and experimentally characterized using scanning electron and atomic force microscopies, X-ray diffraction, and UV-vis-NIR spectroscopy. The morphologic, crystallographic, and optical properties were analyzed. Structural and electronic properties were compared to predictions obtained from computational calculations based on the density functional theory plus U approach (DFT+U). All these simulations provided additional data that could be used as a reference for material modeling and a better understanding of the experimental results. It was found that spray pyrolysis can be used to produce thin film ceramic samples (~300 nm) with low amounts (<5%) of Ni impurities substitutionally located at the cationic sites of the ZnO wurtzite host structure. The results of this investigation showed that an experimental and theoretical study aided in a better characterization of the thin films, and helped to outline a more robust model of the samples.
Keywords: ZnO, thin films, doped ceramics, transmittance, DFT+U.

INTRODUCTION

Zinc oxide (ZnO) is a very promising semiconductor due to its potential applications as a transparent conducting oxide (TCO). ZnO ceramics crystallize in the hexagonal wurtzite structure and attract research interest due to their high availability, excellent chemical and thermal stability, and wide direct bandgap (E_g=3.3 eV) [1]. Its favorable properties as a thin film with high optical transmittance in the visible region make it a permanent candidate for optoelectronic devices, gas sensors, and solar cells, among others [1-3]. In addition, the doping of ZnO with transition metals can enhance the material performance for new applications [4-8]. Regarding the fabrication methods for these compounds as thin films, the increasing demand for devices based on TCOs has promoted the development of different deposition techniques such as sol-gel spin coating, magnetron sputtering, pulsed laser deposition, and spray pyrolysis [9, 10]. Among all these techniques for producing thin films, spray pyrolysis is especially interesting because of its simplicity and low cost [11]. Considering the potential uses of the ZnO-based thin films, a typical experimental characterization includes the morphological, structural, optical, and electronic properties [12, 13]. Material modeling can also bring valuable information to understand the effect of its composition and structure on its general properties. For example, reflectance and transmittance spectra depend on the film thickness and its optical constants. Hence, semi-empirical strategies such as the envelope method proposed by Swanepoel, can be used to evaluate these film properties [14-16]. On the other hand, fully theoretical methods for ceramic modeling at the crystallographic scale can also bring valuable data, such as those methods based on the density functional theory (DFT) [17]. In this sense, considering that it is known that standard DFT underestimates the experimental ZnO bandgap and related properties, many approaches based on DFT have been proposed to improve their predictions [18-21]. Among them, the DFT+U approach has been demonstrated to be accurate enough for the calculation of structural, elastic, and electronic properties in pristine ZnO, making it suitable for more complex systems such as those with impurities and other defects [22-24].

In this paper, samples of ZnO and Ni-doped ZnO were deposited as a coating on a glass substrate by the spray pyrolysis technique. Nickel was chosen as a representative transition metal to assess the capability of the spray pyrolysis technique for its inclusion as a dopant in the ZnO structure. A comprehensive characterization of the produced thin films was performed by different experimental techniques. In particular, the effect of Ni doping on the ceramic coating was studied, and the microscopic and crystallographic scales were analyzed to establish parameters for an effective description of the film properties through its modeling. In addition, the experimental measurements on the ZnO-based ceramic coatings were compared to predictions on pure and Ni-doped ZnO using DFT+U.

MATERIALS AND METHODS

Experimental procedure: ZnO and Ni-doped ZnO samples

*matiast@cetmic.unlp.edu.ar
https://orcid.org/0000-0002-2387-5833

were fabricated using zinc acetate as a Zn source, nickel nitrate as a Ni source, and soda lime glass as a substrate. The substrate was prepared by washing in detergent solution, ethanol, and acetone and dried at 80 °C. For the undoped ZnO film, 4 g of zinc acetate [$Zn(CH_3COO)_2.2H_2O$, Biopack, 99% purity] was introduced in 50 mL of ethanol (Biopack, 99% purity), and 5 mL of acetylacetone (Merk, 99% purity). The mixture was magnetically stirred until a homogenous solution was obtained. Then, the solution was deposited onto the soda lime glass substrate maintained at 400 °C. To this purpose, 16 mL of the solution was manually sprayed using a commercial airbrush (0.2 mm nozzle, pressure <1.5 bar) onto a conventional microscope slide glass (dimensions 70x20x1 mm, at about 20 cm from the airbrush nozzle). The obtained sample was called ZN0. On the other hand, for the fabrication of the Ni-doped ZnO films, nickel nitrate [$Ni(NO_3)_2.6H_2O$, Merk, 99% purity] was added to the above solution with two different concentrations, considering an atomic ratio of Ni to Zn of 2% and 4%. The obtained samples were called ZN2 and ZN4, respectively. In Fig. 1, images of the three samples are shown and compared to the starting glass substrate.
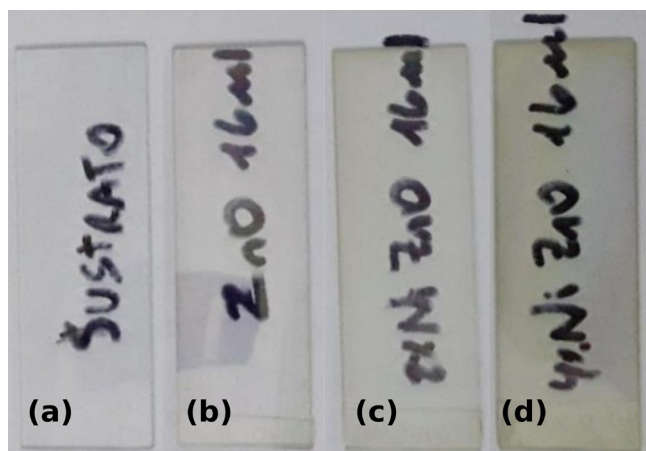

Figure 1: Image of the glass substrate (a) and samples ZN0 (b), ZN2 (c), and ZN4 (d).

The morphology of the samples was characterized using scanning electron microscopy (SEM, Quanta 200, FEI) and atomic force microscopy (AFM, Veeco). SEM was also used to evaluate the film thickness, which required the sample polishing up to optical quality (1/4 μm) with diamond paste. The morphology analysis was complemented by energy dispersive spectrometer (EDS) measurements to assess the chemical composition. The crystalline structure was analyzed by X-ray diffraction (XRD, D2 Phaser, Bruker), from which the lattice parameters, crystallite size, and preferred orientation were determined. Finally, the optical transmittance was studied by UV-vis-NIR spectroscopy (8453 HP, Agilent). This technique allowed the measurement of the film thickness considering the envelope method [15]. Also, for each sample, the bandgap E_g using the Tauc relation was evaluated [25].

Theoretical approach: DFT+U calculations were performed with the open-source Quantum Espresso (QE) code, which is based on pseudopotentials and plane waves [26]. The parameterization of Perdew-Burke-Ernzerhof (PBE) was used for the exchange-correlation function [27]. The starting ZnO wurtzite structure (undoped ZnO, Fig. 2a) was fully optimized and used for the construction of a 2x2x2 supercell in which one Zn atom was substituted by a Ni atom (Ni-doped ZnO, Fig. 2b). This led to a Ni doping concentration of 6.25 at%. In addition, considering that ZnO is naturally an n-type semiconductor, a charged supercell was evaluated by adding 2 electrons to the doped system (charged Ni-doped ZnO). The atomic positions in the three supercells (undoped, Ni-doped, and charge-doped) were refined at the DFT+U level. To this purpose, and considering previous investigations, the PBE functional was complemented by Hubbard U potentials of 6.5 eV on the O-p and Ni-d orbitals, and of 12 eV on the Zn-d orbitals [18, 20, 28]. Converged parameters were obtained using a 3x3x3 k-point mesh in the Monkhorst-Pack scheme and a 100 Ry kinetic energy cut-off. The atomic positions in the structures were relaxed until the forces on atoms were below 0.025 eV/Å. The formation energy Ef of the doped system was calculated as Ef=E(Ni:ZnO)-E(ZnO)+μ(Zn)-μ(Ni), where E(ZnO) and E(Ni:ZnO) are the total energies of undoped ZnO and the Ni-doped system, and μ(Zn) and μ(Ni) are the chemical potentials of the Zn and Ni atoms, which were computed as the energy of bulk Zn and Ni, respectively. For the ZnO and Ni-doped ZnO obtained structures, the Zn-O and Ni-O bond lengths were analyzed and the predicted density of electronic states (DOS) and bandgaps were compared.
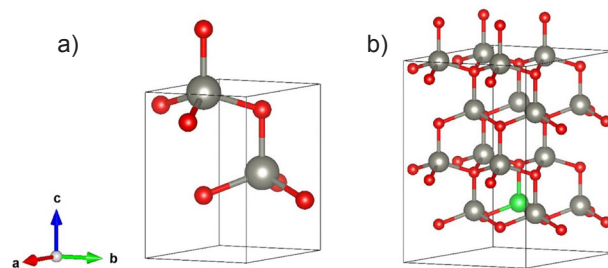

Figure 2: Schematics of a wurtzite ZnO unit cell (a) and Ni-doped ZnO supercell (b). The grey, red, and green balls stand for Zn, O, and Ni atoms, respectively, and the sticks are included to show the cationic tetrahedral environments.

RESULTS AND DISCUSSION

Experimental results

Fig. 3 shows the SEM micrographs of the samples. As can be seen, films without and with Ni content had very similar morphology: they were formed by lenticular grains with sizes of about 100 nm, distributed homogeneously over a surface that did not present serious defects (voids,

pinholes, or cracks). The cross-section micrograph of Fig. 3c was used to determine the thickness of the ZN2 film, assumed to be representative of the other samples. As shown in the figure, from the measurements at different locations of the film, an average thickness of 280 nm was determined. Another look at the film surface
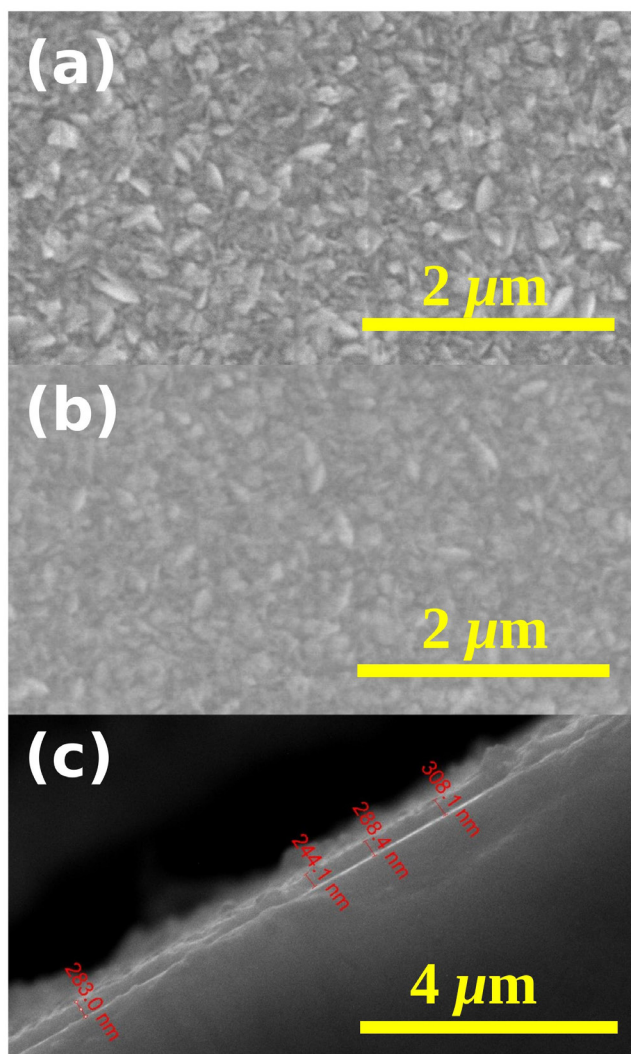

Figure 3: Representative SEM micrographs of: a) ZN0 surface; b) ZN4 surface; and c) ZN2 transverse cross-section.

morphologies was performed using AFM. Fig. 4 presents the AFM images of the three samples that shows that they were composed of well-defined grains homogeneously distributed over the surface, with a nearly uniform density. The film height was characterized by the surface roughness average (Ra), which is the arithmetic average of the absolute values of the roughness profile ordinates. For ZN0, ZN2, and ZN4, Ra took the values 11.6(5), 16.3(5), and 10.8(5) nm, respectively, which represented a height variation up to about 7% of the film thickness determined by SEM.

The composition of the ceramic films was analyzed by EDS. For each sample, the spectra recorded over a 3600 μm^2 area allowed the identification of the atomic species that formed the thin film (Zn, O, and Ni) and the substrate (O, Si, Ca, Na, Mg, and K). Fig. 5a shows the spectrum for the ZN4 sample, and Table I summarizes the quantification of the contents of the main species determined for all samples. The measured Ni to Zn atomic ratio was 0, 0.7%, and 1.4% for ZN0, ZN2, and ZN4, respectively, which was consistent with the Ni content increase in the doped ZnO films. On the other hand, the presence of the elements of the substrate was almost the same in the three samples, indicating that measurement conditions were comparable and also suggesting similar film thicknesses for the three samples. Regarding the element distribution over the film, EDS signal mapping was performed. As an example, Figs. 5b and 5c present a mapping of Zn and Ni signals in the ZN4 sample. As can be seen, the doping atom was homogeneously distributed over the film surface, indicating that there were no Ni clusters in the samples.

Fig. 6 shows the XRD patterns of the three samples. The peaks at 2θ of 31.8°, 34.5°, 36.3°, and 56.6° corresponded to the (100), (002), (101), and (110) planes of the hexagonal wurtzite, respectively. This result showed that all films presented the ZnO wurtzite crystal structure, and no secondary phases were detected when Ni was added (such as nickel or NiO). Using the XRD data, different crystal structural parameters were determined [29]. Lattice parameters a and c were deduced considering Bragg's law, (100) and (002) diffraction
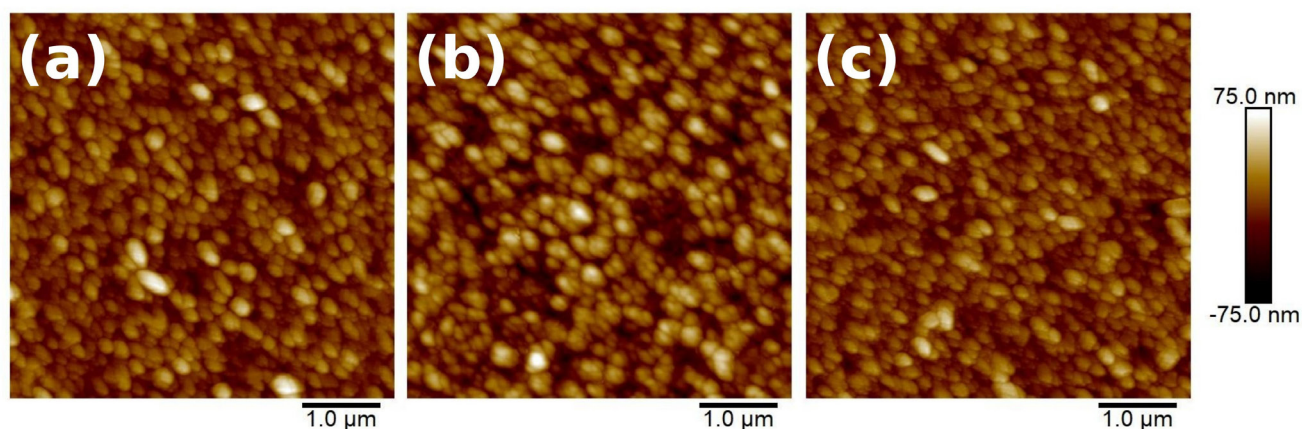

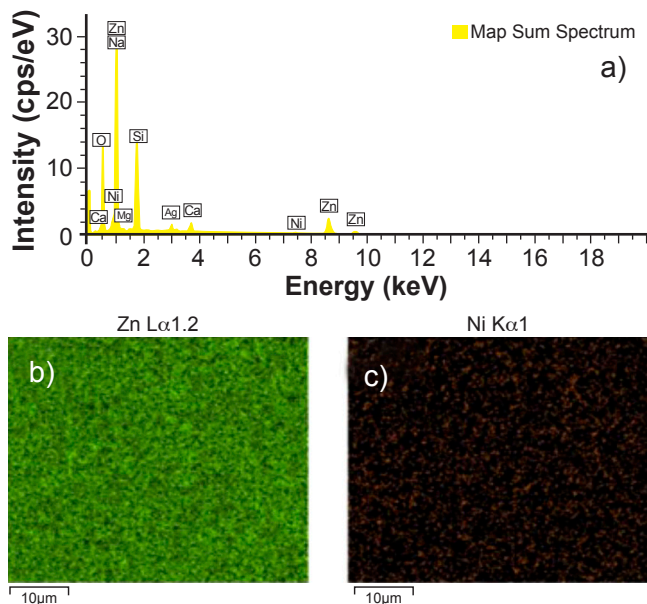Figure 4: AFM images of ZN0 (a), ZN2 (b), and ZN4 (c) sample surfaces.

Figure 5: EDS spectrum (a) and Zn (b) and Ni (c) EDS mapping results for sample ZN4.

peaks, and using the relation:

$$\frac{1}{d_{hkl}^2}=\frac{4(h^2+h.k+h^2)}{3a^2}+\frac{l^2}{c^2} \qquad (A)$$

where d_{hkl} is the inter-planar spacing between hkl planes. In addition, the average value of crystallite size D was estimated

for the samples using the Debye-Scherrer equation:

$$D=\frac{0.9\lambda}{\beta.\cos\theta} \qquad (B)$$

where θ is the diffraction angle, λ is the X-ray wavelength (1.5418 Å for CuKα radiation), and β is the full width at half maximum (FWHM) of the peak. The measured crystal structural parameters for the three samples are presented in Table II and show that no significant changes were detected with increasing Ni content. Also, the obtained values for the lattice parameters were in good agreement with those reported for ZnO by other authors (a=3.253 Å and c=5.205 Å [30]). These results suggested that Ni atoms entered into the wurtzite ZnO lattice and substituted Zn^{2+} forming the mixed oxide Zn$_{(1-x)}$Ni$_x$O without producing significant changes to the host structure.

On the other hand, the strong (002) diffraction peak in Fig. 6 indicated that samples present a preferred growth direction along the c-axis, as also observed by many authors for ZnO coatings produced by different methods [12]. This preferential crystallite orientation was quantitatively analyzed using the texture coefficient (TC), which compares the relative peak intensities with those obtained for polycrystalline ZnO (reference data file JCPDS 36-1451). For each hkl plane, the TC was determined using the relation:

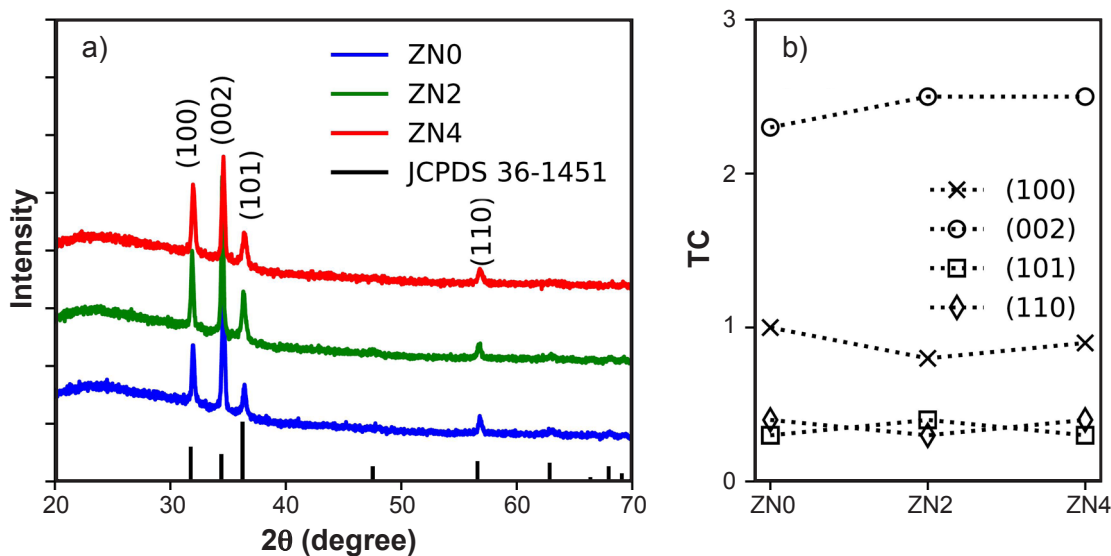$$TC_{hkl}=\frac{N.I_{hkl}/I_{hkl}^0}{\Sigma I_{hkl}/I_{hkl}^0} \qquad (C)$$

Figure 6: XRD patterns (a) and texture coefficients, TC (b), of the prepared samples.

Table I - Composition (at%) of the samples from EDS analysis.

Sample	Zn	Ni	O	Si	Na	Ca	Mg	K
ZN0	14.39	-	67.83	9.11	6.94	1.03	0.64	0.06
ZN2	16.15	0.11	67.33	8.22	6.62	1.01	0.51	0.05
ZN4	17.17	0.24	66.80	7.66	6.68	0.93	0.48	-

Table II - Wurtzite crystal structural parameters a and c and crystallite size D from XRD measurements. Numbers in brackets indicate uncertainty.

Sample	a (Å)	c (Å)	c/a	D (nm)
ZN0	3.235(8)	5.192(8)	1.60	38(3)
ZN2	3.239(1)	5.200(2)	1.60	42(2)
ZN4	3.232(6)	5.189(7)	1.60	39(5)

where I_{hkl} is the measured peak intensity, I_{hkl}^0 is the corresponding peak intensity of the reference file, and N is the number of considered reflection planes from the XRD pattern. Fig. 6b presents the corresponding TC values for the studied samples. It was observed that TC took almost the same values for the three samples, being the (002) plane the one with the highest texture coefficient (TC_{002} ~2.5).

Optical transmittance spectra as a function of wavelength $T(\lambda)$ are presented in Fig. 7a. The three thin films had practically the same threshold wavelength at about 380 nm, which divided the strong absorption region from the weak one. In the visible region, they presented high transmittance (>80%) and reached the maximum values in the infrared region. The presence of oscillations in the transparent region indicated that the film thickness was uniform. Also, the three samples had the same number of interference fringes, which suggested that all had a similar thickness. Because the spectra had the minimum amount of interference fringes, a local approximation of the envelope method was implemented in the transparent spectral region to determine in each case the index of refraction n and thickness t of the ceramic coating. To this purpose, a straight line connecting the contiguous valleys of the spectrum was constructed to evaluate the position of the minimum and maximum transmittance points required by the method proposed by Swanepoel (T_m and T_M, respectively) [15]. Considering a refractive index of the substrate s=1.59, the obtained values

of n and t for the ceramic coatings are presented in Table III. As can be seen, the three samples had very similar values for their refractive index, which are in agreement with those corresponding to ZnO [31]. On the other hand, the film thickness was practically the same for the three samples, and was consistent with the SEM image of Fig. 3c. It must be mentioned that the envelope method applied to the UV-vis-NIS measurements is very sensitive for the thickness determination. As an example of this sensitivity, in Fig. 7a are also presented simulations of the optical transmittance T considering two different values of t and the expression:

$$T(n, x) = \frac{A.x}{B - C.x.\cos\varphi + D.x^2} \quad (D)$$

where $A = 16n^2.s$, $B = (n+1)^3(n+s^2)$, $C = 2(n^2-1)(n^2-s^2)$, $D = (n-1)^3(n-s^2)$, $\varphi = 4\pi.n.t/\lambda$, $x = \exp(-\alpha.t)$ [14], and for the film absorption coefficient $\alpha(\lambda)$ was considered the Beer-Lambert law $\alpha = \ln(1/T)/t$. As can be seen, the simulated spectra imitated the general form of the experimental transmittance $T(\lambda)$ and showed that values of t in the range 240-290 nm can produce visible changes in the interference fringes. The subtle differences between the simulated and measured spectra were attributed to the over-simplified model, which assumed that the sample had a uniform thickness and no inhomogeneities. In this respect, more elaborated models have been proposed to reproduce different particular features of the optical transmittance, which involve film specifications such as their surface roughness and compositional inhomogeneity [32, 33]. Taking into account the above-described morphology of the films, such complex models may exceed the purpose of this paper.

On the other hand, the transmittance spectrum region near the threshold wavelength was used to determine the direct bandgap E_g through the Tauc's relation $\alpha.h\nu = A(h\nu - E_g)^{1/2}$, where $h\nu$ is the photon energy and A is a constant. The obtained results for E_g are included in Table III, which suggested that
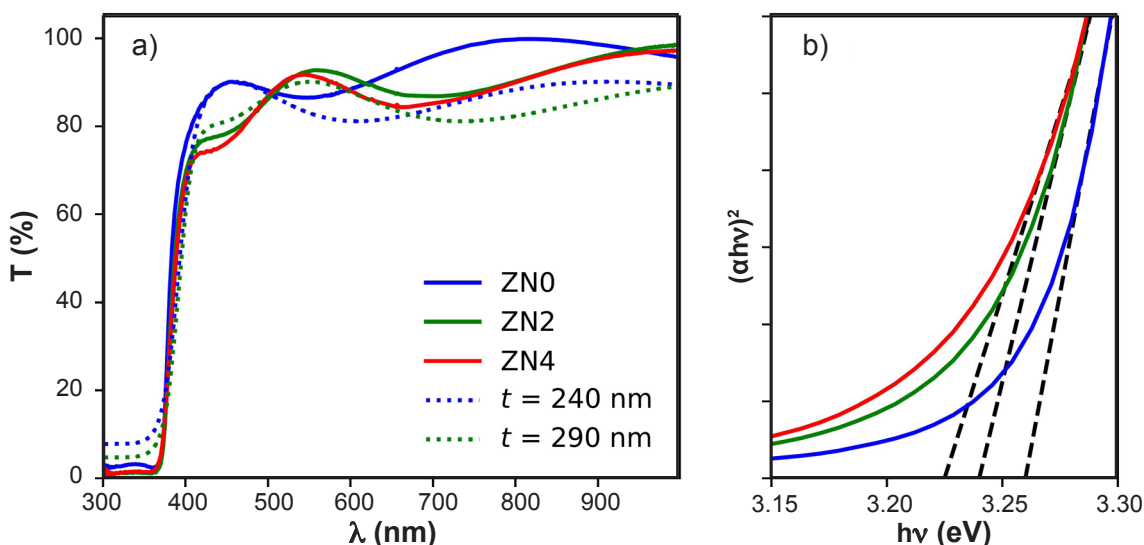

Figure 7: Transmittance spectra (a) and Tauc plot (b) of the studied samples. Dotted lines in (a) correspond to numerical simulations of the transmittance spectra considering different thicknesses t (see text).

Table III - Sample thickness t, refractive index n, and optical bandgap E_g obtained from the transmittance spectra.

Sample	t (μm)	n	E_g (eV)
ZN0	0.30(1)	1.87(1)	3.26(1)
ZN2	0.29(3)	1.92(1)	3.24(1)
ZN4	0.29(3)	1.99(1)	3.22(1)

Ni impurities in the considered amounts did not produce significant changes in E_g (variations were below 2%). The value of E_g obtained for the ZN0 sample was in good agreement with those in the literature for ZnO [2, 31], while those of Ni-doped samples were also consistent with recent investigations in similar films [4, 28, 34, 35].

Theoretical results

The DFT+U method was initially used for predicting the ZnO wurtzite crystal structure. The computed lattice parameters after full optimization of the unit cell were a=3.237 Å and c=5.213 Å (c/a=1.610), which were in very good agreement with the results measured by XRD in the ZN0 undoped sample (Table II). The formation energy of the Ni-doped ZnO was obtained as Ef=0.46 eV, which indicated that the reaction was endergonic. Other authors reported similar results [36, 37], and also showed that the formation energy strongly depends on the presence of other point defects in the ZnO structure, such as vacancies [38, 39]. In particular, it was reported that Ef reaches negative values when Zn vacancies are present in addition to the Ni impurity [37]. This suggests that the real Ni-doped ZnO material is complex and its formation may require other point defects in addition to the substitutional Ni impurity. Considering the purposes of the present work, the structures for undoped and Ni-doped ZnO were kept as simple as possible, and these additional defects were not included. As presented in Fig. 2a, the cations are tetrahedrally coordinated with one apical and three basal O atoms, so the atomic environments can be characterized by the distances d(M-Oa) and d(M-Ob), respectively. In Table IV, the corresponding structural prediction for the considered supercells after the relaxation of the atomic positions with DFT+U is presented. The obtained predictions indicated that the Ni atom induced a slight contraction in its vicinity in comparison to the starting ZnO structure (contractions below 1% of the starting bond length). This result can be considered a consequence of the differences between the involved ionic radii with the cation substitution (0.60 and 0.55 Å for Zn and Ni, respectively) [40]. On the other hand, the additional electrons in the charged Ni-doped case induced the opposite effect, and the bond lengths slightly increased (about 3%) in comparison to the Ni-doped ZnO case. This suggested that those additional electrons were located at the Ni impurity and the increase in d values was due to Coulomb repulsion between neighbor atoms. Therefore, considering only these two systems, it can be concluded that predicting the effect of Ni doping in the

ZnO host structure is not straightforward for real samples. This is in general agreement with the experimental results, which showed that for Ni doping up to 4 at% no compressive or expansive strain was observed through XRD (see lattice parameters in Table II).

Table IV - DFT+U predicted structures and bandgaps E_g for the considered systems. The d distances represent the bond lengths that characterize the cationic environments (M= Zn or Ni).

Structure	$d(M-O_a)$ (Å)	$d(M-O_b)$ (Å)	E_g (eV)
Undoped ZnO	1.982	1.968	3.25
Ni-doped ZnO	1.965	1.963	3.40
Charged Ni-doped ZnO	2.041	2.019	3.30

The calculated density of electronic states (DOS) corresponding to each of the three structures is shown in Fig. 8. The DOS of the pure ZnO structure (in black) presented the known valence band (VB) with O-p and Zn-d characters and the conduction band (CB) with Zn-s and O-p character, both separated by a bandgap of 3.25 eV. This result was in good agreement with the experimental measurement in sample ZN0 (Table III), and reflected the capability of the DFT+U approach, as also reported in previous work [20]. Compared with the pure ZnO DOS, the Ni atom in the Ni-doped ZnO case induced the appearance of impurity levels in the bandgap, and did not significantly change the value of the bandgap (3.40 eV, blue DOS in Fig. 8). The impurity levels had Ni-3d character, and the last of them, about 2 eV above the top of the VB, was partially filled. This indicated that the Ni atom can act as an acceptor impurity in the ZnO matrix, in agreement with the lack of two electrons compared to the Zn atoms it substitutes. When the two electrons were added to the system (red DOS in Fig. 8), then the Fermi level (last occupied energy level) moved towards higher energies. The main difference compared to the Ni-doped ZnO DOS was that impurity levels also moved towards the CB minimum, showing that the charged Ni-doped ZnO system incorporated the two electrons to the Ni-3d orbital and also acquired a partial delocalization due to the hybridization of these levels with the O-p orbitals that compose the bottom of the CB.

The DOS of Fig. 8 shows that including the Ni atom in the ZnO host structure practically did not modify the electronic bandgap, in very good agreement with the transmittance measurements in the ceramic samples (Table IV). On the other hand, from the comparison of the predictions to other recent investigations that involve the DFT+U approach in Ni-doped systems, it is concluded that details in the DOS description depend on the choice of the semiempirical U potentials and also on the Ni concentration [24, 28, 41]. In particular, providing an accurate enough prediction about how the impurity levels are placed within the bandgap is difficult. As a consequence, describing
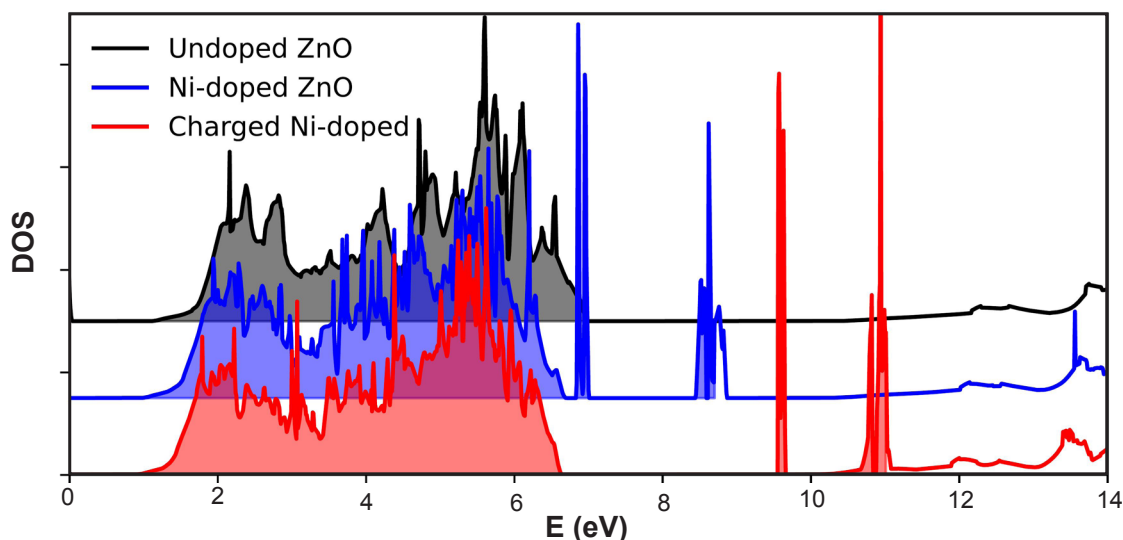
Figure 8: Calculated DOS for ZnO and Ni-doped ZnO structures. In each case, shaded areas indicate occupied energy states.

from theoretical calculations the electronic structure of the experimentally synthesized Ni-doped ZnO material is a difficult task because of its complexity. Nevertheless, among the electronic insights that the DFT+U approach provided in this investigation, it can be highlighted that the Ni impurity states depend on the charge state of the system, which may vary in the material due to the n-type semiconductor nature of the ZnO host structure.

CONCLUSIONS

ZnO and Ni-doped ZnO ceramic thin films were successfully prepared by spray pyrolysis. The experimental characterization indicated that this technique can be used to substitutionally locate the impurities at the cationic sites of the ZnO wurtzite host structure, with no additional segregated phases. The ZnO thin films grew with a preferred orientation along the direction (002), and the doping with low amounts of Ni impurities (<5%) did not substantially affect the film morphology, formed by lenticular grains, nor its uniform thickness (~300 nm) and electronic bandgap (~3.25 eV). Overall, the results of this investigation showed that the use of experimental complementary techniques, the optical transmittance simulation, and the DFT+U predictions for the crystallographic and electronic properties aided in a better characterization of the thin films, and helped to outline a more robust model of the samples. The obtained results encourage further studies using these methodologies on other doped thin films, considering higher impurity concentrations and other transition metals as dopants. Some of these investigations are now in progress.

ACKNOWLEDGEMENTS

REFERENCES

[1] J. Theerthagiri, S. Salla, R.A. Senthil, P. Nithyadharseni, A. Madankumar, P. Arunachalam, T. Maiyalagan, H.S. Kim, Nanotechnology **30** (2019) 392001.
[2] H. Ennaceri, M. Boujnah, D. Erfurt, J. Rappich, X. Lifei, A. Khaldoun, A. Benyoussef, A. Ennaoui, A. Taleb, Sol. Energy Mater. Sol. Cells **201** (2019) 110058.
[3] M. Zayed, A.M. Ahmed, M. Shaban, Int. J. Hydrog. Energy **44** (2019) 17630.
[4] S. Rajeh, A. Mhamdi, K. Khirouni, M. Amlouk, S. Guermazi, Opt. Laser Technol. **69** (2015) 113.
[5] V.D. Mote, Y. Purushotham, R.S. Shinde, S.D. Salunke, B.N. Dole, Cerâmica **61**, 360 (2015) 457.
[6] A. Morais, R.A. Torquato, U.C. Silva, C. Salvador, C. Chesman, Cerâmica **64**, 372 (2018) 627.
[7] J.S.C. Licurgo, G.R. de Almeida Neto, H.R. Paes Junior, Cerâmica **66**, 379 (2020) 284.
[8] D.B. Maia, R.A. Raimundo, T.A. Passos, R.A. Torquato, Cerâmica **66**, 379 (2020) 262.
[9] J. Leng, Z. Wang, J. Wang, H.H. Wu, G. Yan, X. Li, H. Guo, Y. Liu, Q. Zhang, Z. Guo, Chem. Soc. Rev. **48** (2019) 3015.
[10] P.J. McGinn, ACS Comb. Sci. **21** (2019) 501.
[11] S.R. Sriram, S.R. Parne, N. Pothukanuri, D.R. Edla, J. Anal. Appl. Pyrolysis **164** (2022) 105527.
[12] L. Znaidi, Mater. Sci. Eng. B **174** (2010) 18.
[13] M.T. Noman, N. Amor, M. Petru, Crit. Rev. Solid State Mater. Sci. **47** (2022) 99.

[14] R. Swanepoel, J. Phys. Sci. Instrum. **16** (1983) 1214.

[15] D. Dorranian, L. Dejam, G. Mosayebian, J. Theor. Appl. Phys. **6** (2012) 13.

[16] Y. Jin, B. Song, Z. Jia, Y. Zhang, C. Lin, X. Wang, S. Dai, Opt. Express **25** (2017) 440.

[17] P. Makkar, N.N. Ghosh, RSC Adv. **11** (2021) 27897.

[18] E.S. Goh, J.W. Mah, T.L. Yoon, Comput. Mater. Sci. **138** (2017) 111.

[19] K. Bashyal, C.K. Pyles, S. Afroosheh, A. Lamichhane, A.T. Zayak, J. Phys. Condens. Matter **30** (2018) 65501.

[20] A. Apaolaza, D. Richard, M.R. Tejerina, Process. Appl. Ceram. **14** (2020) 362.

[21] K. Harun, N. Azmira Salleh, B. Deghfel, M. Kamil Yaakob, A. Azmin Mohamad, Results Phys. **16** (2020) 102829.

[22] M.V. Gallegos, C.R. Luna, M.A. Peluso, L.C. Damonte, J.E. Sambeth, P.V. Jasen, J. Alloys Compd. **795** (2019) 254.

[23] E. Benrezgua, A. Zoukel, B. Deghfel, Z. Boukhari, R. Amari, S. Kheawhom, A. Azmin Mohamad, Mater. Today Commun. **31** (2022) 103306.

[24] M. Ramzan, M.A. Moiz, M.B. Khalid, S.W. Husain, Mater. Today Commun. **33** (2022) 104181.

[25] B.D. Viezbicke, S. Patel, B.E. Davis, D.P. Birnie III, Phys. Status Solidi B **252** (2015) 1700.

[26] P. Giannozzi, O. Andreussi, T. Brumme, O. Bunau, M.B. Nardelli, M. Calandra, R. Car, C. Cavazzoni, D. Ceresoli, M. Cococcioni, N. Colonna, I. Carnimeo, A. Dal Corso, S. de Gironcoli, P. Delugas, R.A. DiStasio Jr., A. Ferretti, A. Floris, G. Fratesi, G. Fugallo, R. Gebauer, U. Gerstmann, F. Giustino, T. Gorni, J. Jia, M. Kawamura, H.-Y. Ko, A. Kokalj, E. Küçükbenli, M. Lazzeri, M. Marsili, N. Marzari, F. Mauri, N.L. Nguyen, H.-V. Nguyen, A. Otero-de-la-Roza, L. Paulatto, S. Poncé, D. Rocca, R. Sabatini, B. Santra, M. Schlipf, A.P. Seitsonen, A. Smogunov, I. Timrov, T. Thonhauser, P. Umari, N. Vast, X. Wu, S. Baroni, J. Phys.

Condens. Matter **29** (2017) 465901.

[27] J.P. Perdew, K. Burke, M. Ernzerhof, Phys. Rev. Lett. **77** (1996) 3865.

[28] I. Benaicha, J. Mhalla, A. Raidou, A. Qachaou, M. Fahoume, Materialia **15** (2021) 101015.

[29] G. Vijayaprasath, R. Murugan, G. Ravi, T. Mahalingam, Y. Hayakawa, Appl. Surf. Sci. **313** (2014) 870.

[30] A. Yildiz, B. Kayhan, B. Yurduguzel, A.P. Rambu, F. Iacomi, S. Simon, J. Mater. Sci. Mater. Electron. **22** (2011) 1473.

[31] A. Ashour, M.A. Kaid, N.Z. El-Sayed, A.A. Ibrahim, Appl. Surf. Sci. **252** (2006) 7844.

[32] R. Swanepoel, J. Phys. E **17** (1984) 896.

[33] F. Lai, Y. Wang, M. Li, H. Wang, Y. Song, Y. Jiang, Thin Solid Films **515** (2007) 4763.

[34] D. Iskenderoğlu, H. Güney, Ceram. Int. **43** (2017) 16593.

[35] V.A. Owoeye, E. Ajenifuja, E.A. Adeoye, G.A. Osinkolu, A.P. Popoola, Mater. Res. Express **6** (2019) 86455.

[36] B. Leedahl, D.A. Zatsepin, D.W. Bukhvalov, E.Z. Kurmaev, R.J. Green, I.S. Zhidkov, S.S. Kim, L. Cui, N.V. Gavrilov, S.O. Cholakh, A. Moewes, J. Phys. Chem. C **118** (2014) 28143.

[37] Q. Hou, Z. Xu, X. Jia, C. Zhao, J. Appl. Phys. **123** (2018) 55106.

[38] F. Wang, Z. Pang, L. Lin, S. Fang, Y. Dai, S. Han, J. Magn. Magn. Mater. **321** (2009) 3067.

[39] J.B. Yi, C.C. Lim, G.Z. Xing, H.M. Fan, L.H. Van, S.L. Huang, K.S. Yang, X.L. Huang, X.B. Qin, B.Y. Wang, T. Wu, L. Wang, H.T. Zhang, X.Y. Gao, T. Liu, A.T.S. Wee, Y.P. Feng, J. Ding, Phys. Rev. Lett. **104** (2010) 137201.

[40] R.D. Shannon, Acta Cryst. A **32** (1976) 751.

[41] H. Ahmoum, G. Li, Y. Piao, S. Liu, R. Gebauer, M. Boughrara, M.S. Su'ait, M. Kerouad, Q. Wang, J. Alloys Compd. **854** (2021) 157142.